



Article

Fabrication of Nano Iron Oxide–Modified Biochar from Co-Hydrothermal Carbonization of Microalgae and Fe(II) Salt for Efficient Removal of Rhodamine B

Ziling Peng, Zeyu Fan ^{*}, Xia Chen ^{*}, Xian Zhou, Zhuo Fan Gao, Shanshan Deng, Sha Wan, Xingdong Lv, Yan Shi and Wei Han

Changjiang River Scientific Research Institute, Research Center of Water Engineering Safety and Disaster Prevention of Ministry of Water Resources, Wuhan 430010, China; pengziling0304@163.com (Z.P.); zhouxian@mail.crsri.cn (X.Z.); gaofz@mail.crsri.cn (Z.F.G.); dengss@mail.crsri.cn (S.D.); wansha@whu.edu.cn (S.W.); lvxingdong9010@126.com (X.L.); 18163559730@163.com (Y.S.); hanwei@mail.crsri.cn (W.H.)

^{*} Correspondence: fanzeyu717728@163.com (Z.F.); chenxia@mail.crsri.cn (X.C.)

Abstract: Dye adsorption by magnetic modified biochar has now received growing interest due to its excellent adsorption performance and facile separation for recycling. In this study, nano iron oxide–modified biochar was fabricated via the successive hydrothermal-pyrolyzing method using *Chlorella vulgaris* (Cv) and FeSO₄·7H₂O as raw materials, and its adsorption on Rhodamine B (RhB) in aqueous solution was studied. Multiple techniques such as X-ray diffraction (XRD), Fourier transform infrared spectroscopy (FTIR), scanning electron microscopy (SEM), transmission electron microscopy (TEM), Brunauer–Emmett–Teller (BET), vibrating sample magnetometry (VSM) and X-ray photoelectron spectroscopy (XPS) were employed to comprehensively characterize the structure, morphology and physicochemical properties of the adsorbent. The as-synthesized nano iron oxide–modified biochar (CBC-Fe(II)) exhibited a large surface area (527.6 m²/g) and high magnetic saturation value (13.7 emu/g) to facilitate magnetic separation. Compared with CBC and CBC-Fe(III), CBC-Fe(II) exhibited superior adsorption ability towards RhB in aqueous solution, with a maximum adsorption capacity of 286.4 mg/g. The adsorption process of RhB onto CBC-Fe(II) was well described by the pseudo-second-order kinetic model and Langmuir isotherm model, indicating monolayer chemisorption behaviors for the adsorption system. Facile preparation, great adsorption performance and magnetic recovery properties endow CBC-Fe(II) to be a promising adsorbent for dye removal.

Keywords: nano iron oxide; biochar; magnetic; Rhodamine B; adsorption



Citation: Peng, Z.; Fan, Z.; Chen, X.; Zhou, X.; Gao, Z.F.; Deng, S.; Wan, S.; Lv, X.; Shi, Y.; Han, W. Fabrication of Nano Iron Oxide–Modified Biochar from Co-Hydrothermal Carbonization of Microalgae and Fe(II) Salt for Efficient Removal of Rhodamine B. *Nanomaterials* **2022**, *12*, 2271. <https://doi.org/10.3390/nano12132271>

Academic Editor: Diego Cazorla-Amorós

Received: 10 June 2022

Accepted: 28 June 2022

Published: 1 July 2022

Publisher's Note: MDPI stays neutral with regard to jurisdictional claims in published maps and institutional affiliations.



Copyright: © 2022 by the authors. Licensee MDPI, Basel, Switzerland. This article is an open access article distributed under the terms and conditions of the Creative Commons Attribution (CC BY) license (<https://creativecommons.org/licenses/by/4.0/>).

1. Introduction

Recently, the content of organic pollutants in the environment has been increasing due to the rapid development of industry, leading to severe environmental issues [1–4]. Specifically, the disposed water from the textile, printing, cosmetics, medicine and other industries contains a significantly high amount of organic dye molecules which are potentially carcinogenic and teratogenic with high toxicity, posing a serious threat to various organisms and human health [5,6]. Therefore, developing an efficient technology to remove those dye contaminates from wastewater is indispensable to prevent environmental pollution.

A variety of treatment techniques have been utilized for the removal of dyes from polluted water, including coagulation [7], flocculation [8], oxidation [9], adsorption [10], electrochemical separation [11], microbiological decomposition [12] and the membrane process [13]. Among all, adsorption has become one of the most widely used methods due to its advantages of low cost, high efficiency, simple operation and environment-friendliness [14–16]. Some adsorbents developed for removing dyes from wastewater

include bentonite [17], graphene [18], activated carbon [19], etc., and research is still going on to develop more economical, sustainable and efficient materials as new adsorbents for dye removal.

Biochar (BC), a carbon-based porous product obtained from the pyrolysis of biomass and possesses high potential for dye pollution remediation owing to its renewability, stability, its various sources, environmental sustainability and its beneficial physicochemical properties, including high surface area, developed pore structure, and others [20,21]. The renewable resources can be easily obtained from agricultural waste or naturally abundant biomass such as fruit peels, coconut shells, cassava slag, rice husk, sewage sludge, macroalgae, microalgae, etc. [22–24]. Wu et al. [25] prepared biochar from agricultural waste cassava slag by hydrothermal carbonization treatment, and the cassava slag biochar had excellent adsorption performance on RhB with a maximum adsorption capacity of 105.3 mg/g. Hou et al. [26] synthesized biochar with well-developed pores using agricultural waste from bamboo shoot shells as the raw materials. The biochar produced at the carbonization temperature of 800 °C could efficiently remove RhB from water. Vigneshwaran et al. [27] fabricated sulfur-doped biochar derived from tapioca peel waste, which had the adsorption capacity of 30.18 and 33.10 mg/g for malachite green and RhB dye, respectively. Nevertheless, the adsorption capacity of the above reported biochar is relatively limited. Moreover, solid–liquid separation often requires complementary steps of centrifugation and filtration, restraining its application potential.

In this case, biochar activated by magnetic modification exhibits controlled movement under an external magnetic field, making it easy to separate [28]. Magnetic biochars are fabricated by chemically combining them with other functional elements such as Fe, Fe₃O₄, γ-Fe₂O₃, CoFe₂O₄, etc., which leads to strong metal binding [29–31]. Though magnetic biochar has the advantage of easy separation, the surface pores are prone to be plugged with those functional particles, causing a decrease in its adsorption efficiency [32]. In addition, Fe-modified biochar is widely applied in the advanced oxidation process and the adsorption of heavy metal ions, but there are few studies involving adsorption of dyes by Fe-modified biochar [33]. Therefore, it is essential to explore a facile method to fabricate magnetic biochar adsorbents for dye removal and improve adsorption properties of biochar in the meantime.

Herein, nano iron oxide–modified biochar was successfully prepared via successive hydrothermal and pyrolyzing treatments. One of the easily cultivated microalgae (Cv) was selected as carbonaceous feedstock in this work owing to the wide abundance, high biomass productivity as well as the technical challenges associated with its treatment and disposal [34–36]. The obtained nano iron oxide–modified biochar was analyzed via XRD, FTIR, SEM, TEM, BET, VSM and XPS techniques. RhB, as a representative cationic organic dye compound, is considered to be more difficult to remove due to the high solubility in water [37,38]. Thus, RhB dye was chosen as the target contaminant to assess the adsorption efficiency of the nano iron oxide–modified biochar. The influence of adsorbent dosage, initial RhB concentration, adsorption time and temperature on the adsorption performance was also examined. The mechanism of RhB adsorption was further analyzed via kinetic and isothermal models. The results of this study offer a new approach to dye wastewater treatment using nano iron oxide–modified biochar and explore a new way for the resource utilization of Cv.

2. Materials and Methods

2.1. Materials

Cv powder was obtained from Xi'an Youshuo Biotechnology Co., Ltd. (Xi'an, China) Iron(II) sulfate heptahydrate (FeSO₄·7H₂O), iron(III) nitrate nonahydrate (Fe(NO₃)₃·9H₂O), nitric acid (HNO₃), ethanol (C₂H₅OH) and RhB were all supplied by Sinopharm Chemical Reagent Co., Ltd. (Shanghai, China) All chemical reagents were of analytical grade and were used without further purification. Ultrapure water (18.25 MΩ·cm) was used in all the experiments.

2.2. Preparation of Adsorbents

2.2.1. Preparation of Biochar

The *Chlorella*-derived biochar (CBC) was prepared through pyrolyzing the carbonaceous precursor (Cv). First, the Cv powder was dried at 60 °C overnight. Then the dried precursor was heated at 5 °C/min to 900 °C in a tubular furnace under nitrogen atmosphere and carbonized for 1 h. After cooling to room temperature, the obtained product was ground in a ball mill for 8 h. Finally, the powder was washed separately with HNO₃, absolute ethyl alcohol and ultrapure water and then dried at 60 °C to obtain pure CBC.

2.2.2. Preparation of Nano Iron Oxide–Modified Biochar

Nano iron oxide–modified biochar was prepared via successive hydrothermal-pyrolyzing method. Two kinds of iron salts with different valences (FeSO₄·7H₂O and Fe(NO₃)₃·9H₂O) were selected as iron sources. First, a certain amount of Cv powder was dispersed in a FeSO₄·7H₂O solution under continuous stirring in nitrogen atmosphere. The mass ratio of Fe element to Cv was fixed at 1:6. The mixture was then placed into a Teflon-lined autoclave and hydrothermally treated at 150 °C for 24 h. After the resulting product was dried at 60 °C, it was pyrolyzed at 900 °C using a similar procedure as preparing CBC. Then the obtained product was ball milled for 8 h. Additionally, to remove metallic and organic impurities, the powder was washed separately with HNO₃, absolute ethyl alcohol and ultrapure water. At last, the sample was dried at 60 °C to yield nano iron oxide–modified biochar, which was denoted as CBC-Fe(II). For comparison, CBC-Fe(III) was also prepared with the similar procedure using the iron salt of Fe(NO₃)₃·9H₂O instead of FeSO₄·7H₂O.

2.3. Characterizations

The obtained samples were characterized by XRD analysis on D8 advance X-ray diffractometer (Bruker AXS, Karlsruhe, Germany) with filtered Cu K α radiation. The functional groups of the samples were analyzed by FTIR (Thermo Scientific, Nicolet 67000, Madison, WI, USA). The detailed microstructure and morphology of samples were observed using SEM (ZEISS Gemini SEM 300, Oberkochen, Germany) and TEM (FEI Tecnai F20, Hillsboro, OR, USA). Nitrogen adsorption–desorption isotherms were recorded by Micromeritics ASAP 2460 adsorption apparatus at 77 K (ASAP 2460, Micromeritics, Norcross, GA, USA). The magnetic property of the sample was measured using VSM (LakeShore, Westerville, OH, USA). XPS was conducted at room temperature on an ESCALAB Xi+ instrument (Thermo Fisher Scientific, Waltham, MA, USA) equipped with an Al K α source.

2.4. Adsorption of RhB

The adsorption experiments were carried out in a thermostated mechanical shaker and the speed was set at 200 rpm. A certain amount of the prepared adsorbents was added to 25 mL of RhB dye solution in a 50 mL centrifuge tube. The effects of adsorbent dosage (0–50 mg), adsorption time (0–180 min), temperature (15–35 °C) and initial concentration (100–1500 mg/L) on adsorption were examined. After the adsorption experiment, about 3 mL of the mixture was sampled and filtered through a 0.45 mm membrane filter. The concentration of RhB was determined using Lambda 365 UV/Vis spectrophotometer (PerkinElmer, Waltham, MA, USA) at a wavelength of 554 nm. The removal efficiency R (%), the quantity of RhB adsorbed on the adsorbent Q_t (mg/g) and adsorption capacity Q_e (mg/g) were calculated using Equations (1)–(3).

$$R\% = \frac{C_0 - C_t}{C_0} \times 100\% \quad (1)$$

$$Q_t(\text{mg/g}) = \frac{C_0 - C_t}{m} \times V \quad (2)$$

$$Q_e(\text{mg/g}) = \frac{C_0 - C_e}{m} \times V \quad (3)$$

where C_0 (mg/L) is the initial concentration, C_t (mg/L) is residual concentration at certain time and C_e (mg/L) is the equilibrium concentration; V (L) is the volume of dye solution and m (g) is the mass of adsorbent. To guarantee the reliability of data, all of the above experiments were performed in triplicate.

3. Results and Discussion

3.1. Characterizations of the Synthesized Biochars

The XRD patterns of CBC, CBC-Fe(III) and CBC-Fe(II) are shown in Figure 1a. The broad diffraction peak at about 25° confirmed the presence of amorphous biochar in the three samples [39]. However, only the sample of CBC-Fe(II) showed the peaks related to iron oxide, which were identified as Fe_3O_4 and $\alpha\text{-Fe}_2\text{O}_3$. Specifically, the diffraction peaks at $2\theta = 35.1^\circ, 41.4^\circ, 50.4^\circ, 62.9^\circ, 67.2^\circ$ and 74.1° corresponded to the (220), (311), (400), (422), (511) and (440) planes of Fe_3O_4 , respectively. The diffraction peaks at $2\theta = 38.7^\circ, 41.4^\circ, 47.8^\circ, 58.2^\circ$ and 63.7° corresponded to the (104), (110), (113), (024) and (116) planes of $\alpha\text{-Fe}_2\text{O}_3$, respectively. The results implied that during the process of successive hydrothermal-pyrolyzing, the addition of Fe(II) salt promoted the formation of iron oxide particles, whereas the addition of Fe(III) salt had no positive effect on the formation of iron species in the biochar.

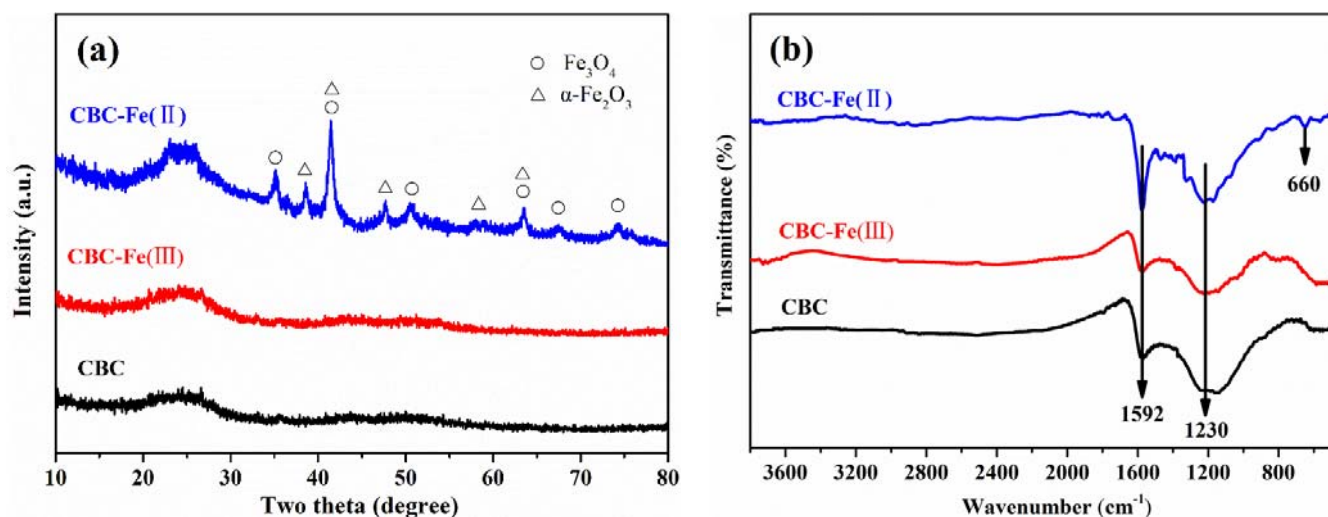


Figure 1. (a) XRD patterns and (b) FTIR spectrum of CBC, CBC-Fe(III) and CBC-Fe(II).

The functional groups of CBC, CBC-Fe(III) and CBC-Fe(II) were determined by FTIR spectra and are shown in Figure 1b. For the three samples, the peaks at 1592 cm^{-1} were attributed to the aromatic C=C groups stretching variations [27,40]. The peaks at 1230 cm^{-1} corresponded to the C–O stretching vibration [41,42]. Notably, the representative absorption bands for the stretching Fe–O band at around 660 cm^{-1} appeared for the sample of CBC-Fe(II) [43,44], further confirming that iron oxides had been successfully modified onto biochar.

Figure 2 shows the typical morphologies of CBC, CBC-Fe(III) and CBC-Fe(II). It can be seen that the surface morphologies of biochars were obviously different. Compared with CBC-Fe(III) and CBC-Fe(II), CBC exhibited larger carbon particles. It was due to the fact that the modification of Fe could prevent the aggregation of carbon particles during biomass carbonization process. It can be seen that some nanostructured particles were observed for the sample of CBC-Fe(II), which could be attributed to the formation of nan iron oxides particles. TEM images of CBC-Fe(II) (Figure 3a,b) revealed that Fe_3O_4 and $\alpha\text{-Fe}_2\text{O}_3$ nanoparticles were presented in biochar. Those nano iron oxides could give more active sites to the prepared biochar, which was in favor of dye adsorption. Figure 3b shows the exhibited characteristic fringes with lattice spacing of 0.253 nm and 0.270 nm , which

could be indexed as the (311) plane of Fe_3O_4 and (104) plane of $\alpha\text{-Fe}_2\text{O}_3$, respectively. The result was consistent with the results of XRD analysis as mentioned above.

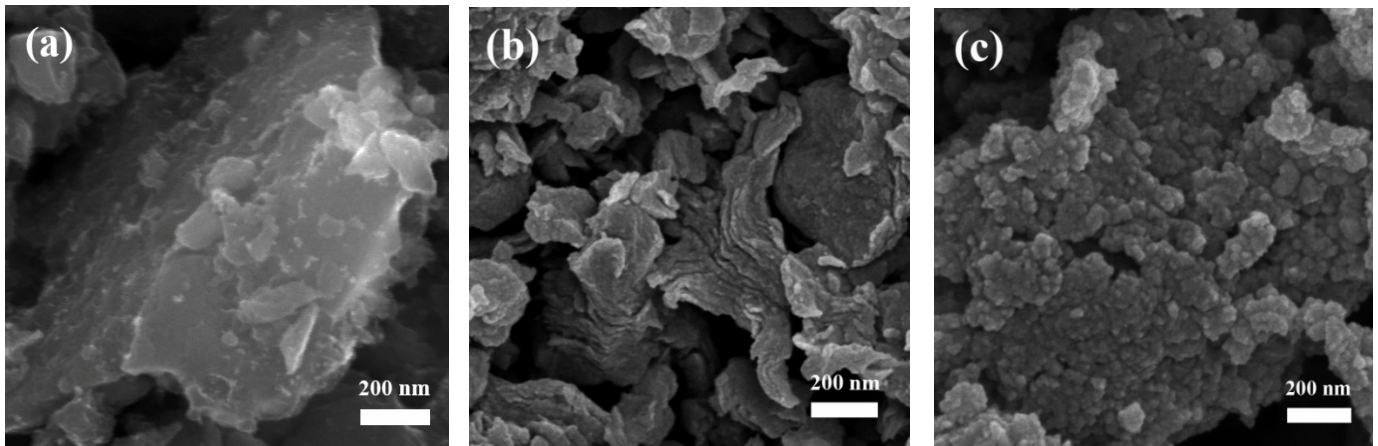


Figure 2. SEM images of (a) CBC, (b) CBC-Fe(III) and (c) CBC-Fe(II).

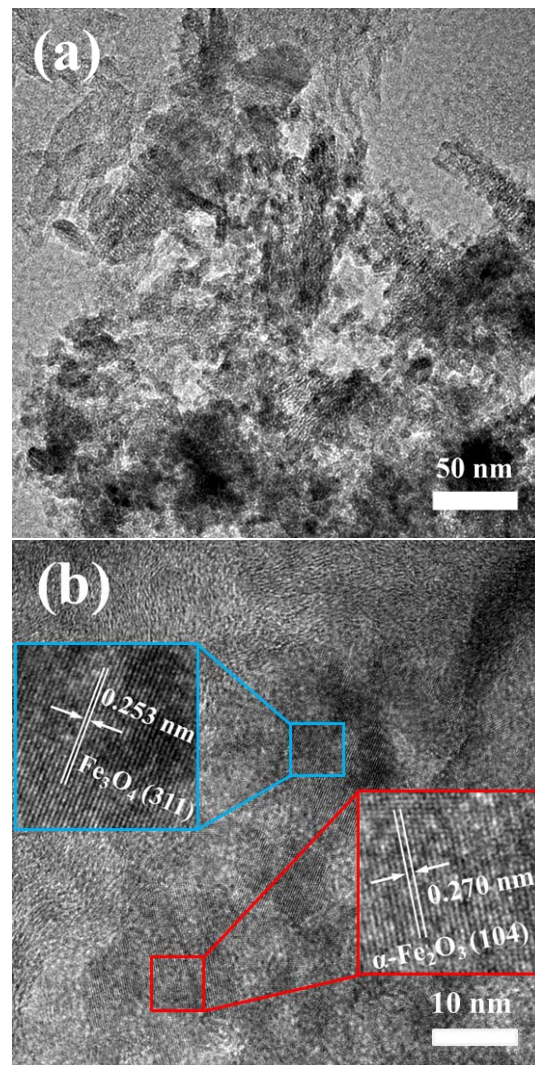


Figure 3. (a) TEM and (b) HRTEM images of CBC-Fe(II).

N_2 adsorption-desorption isotherms of CBC, CBC-Fe(III) and CBC-Fe(II) were detected and are shown in Figure 4a, and calculated pore parameters are summarized in Table 1. According to IUPAC classification, N_2 adsorption-desorption isotherms of the three samples could be classified as type IV, which indicated that the mesoporous structure existed in the biochars. BET surface areas calculated were 338.6, 350.2 and 527.6 m^2/g for CBC, CBC-Fe(III) and CBC-Fe(II), respectively. Notably, compared with CBC and CBC-Fe(III), the BET surface area of CBC-Fe(II) significantly increased. It was due to the fact that the pore structure was increased by the iron oxides formed on CBC-Fe(II). The high specific surface area for CBC-Fe(II) suggested the abundant accessibility of active sites on the adsorbent surface, which could be accountable for an increase in the adsorption efficiency for dye removal. As seen in Table 1, the average pore sizes of CBC, CBC-Fe(III) and CBC-Fe(II) were 4.855, 5.702 and 3.614 nm, respectively, which implied that the prepared samples were mesoporous materials with a certain amount of microporous structure. The result was consistent with the pore size distributions in Figure 4b. It was also observed in Table 1 that CBC-Fe(II) possessed the highest total pore volume and micropore volume compared with the other two samples, further confirming the porous property of CBC-Fe(II).

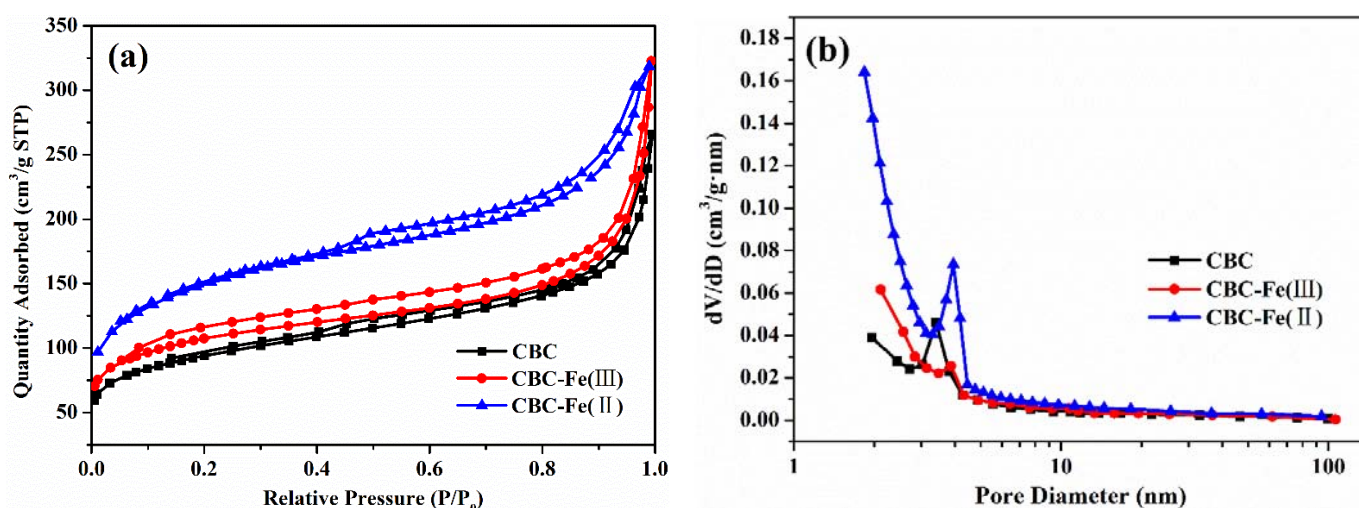


Figure 4. (a) N_2 adsorption-desorption isotherms and (b) pore size distributions of CBC, CBC-Fe(III) and CBC-Fe(II).

Table 1. BET surface area and pore parameters of CBC, CBC-Fe(III) and CBC-Fe(II).

Sample	S_{BET} (m^2/g)	S_{micro} (m^2/g)	V_{total} (cm^3/g)	V_{micro} (cm^3/g)	$D_{average}$ (nm)
CBC	338.6	33.6	0.411	0.010	4.855
CBC-Fe(III)	350.2	99.9	0.477	0.057	5.702
CBC-Fe(II)	527.6	169.3	0.499	0.073	3.614

The magnetic behavior of the CBC-Fe(II) adsorbent was studied. The magnetic hysteresis curves (Figure 5) show that the saturation magnetization (M_s) of CBC-Fe(II) was determined to be 13.7 emu/g. It was concluded that the magnetization of CBC-Fe(II) was high enough to be magnetically collected simply by a magnet.

The XPS spectra of CBC-Fe(II) adsorbent were obtained and are shown in Figure 6. All of the peaks of the scan survey spectra in Figure 6a were ascribed to C, O and Fe elements. The deconvolutions of the C1s spectra of CBC-Fe(II) are shown in Figure 6b. The strongest peak located at 284.8 eV could be assigned to C-C. The other peaks at 285.2 and 285.9 eV corresponded to C-O and C=O functional groups, respectively [45]. Figure 6c represents the XPS spectra of Fe 2p. The peaks at 710.9 and 724.6 eV were respectively ascribed to $2p_{3/2}$ and $2p_{1/2}$ of Fe(II), whereas the peaks at 712.6 and 726.3 eV corresponded to $2p_{3/2}$

and $2p_{1/2}$ of Fe(III) [46]. The peak at 719.5 eV was attributed to the binding energy of the shake-up satellite [47]. The above results verified the existence of Fe_2O_3 and Fe_3O_4 in the sample of CBC-Fe(II), which was consistent with the XRD results. Figure 6d shows that the O1s peak was asymmetric and can be fitted into three peaks. The lowest peak, located at 530.3 eV, was ascribed to the lattice oxygen (O^{2-}) of Fe_2O_3 or Fe_3O_4 in the CBC-Fe(II) sample [48]. The peak centered at 531.8 eV was attributed to C=O in the composite, while the highest peak, at 533.0 eV, was associated with C–O in the composite [45].

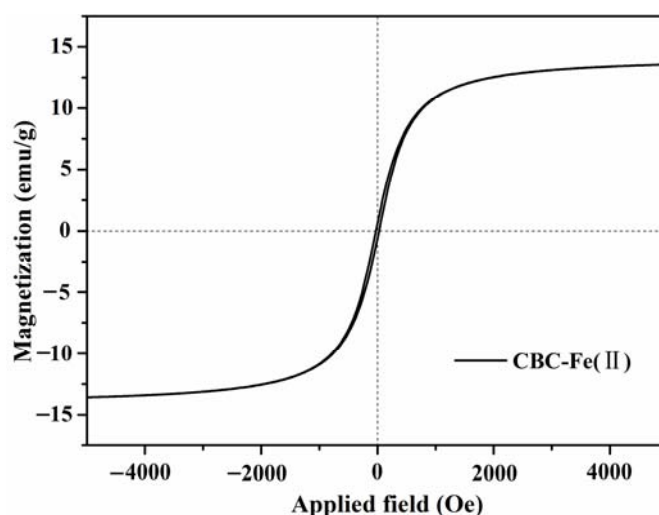


Figure 5. Magnetic hysteresis curves of CBC-Fe(II).

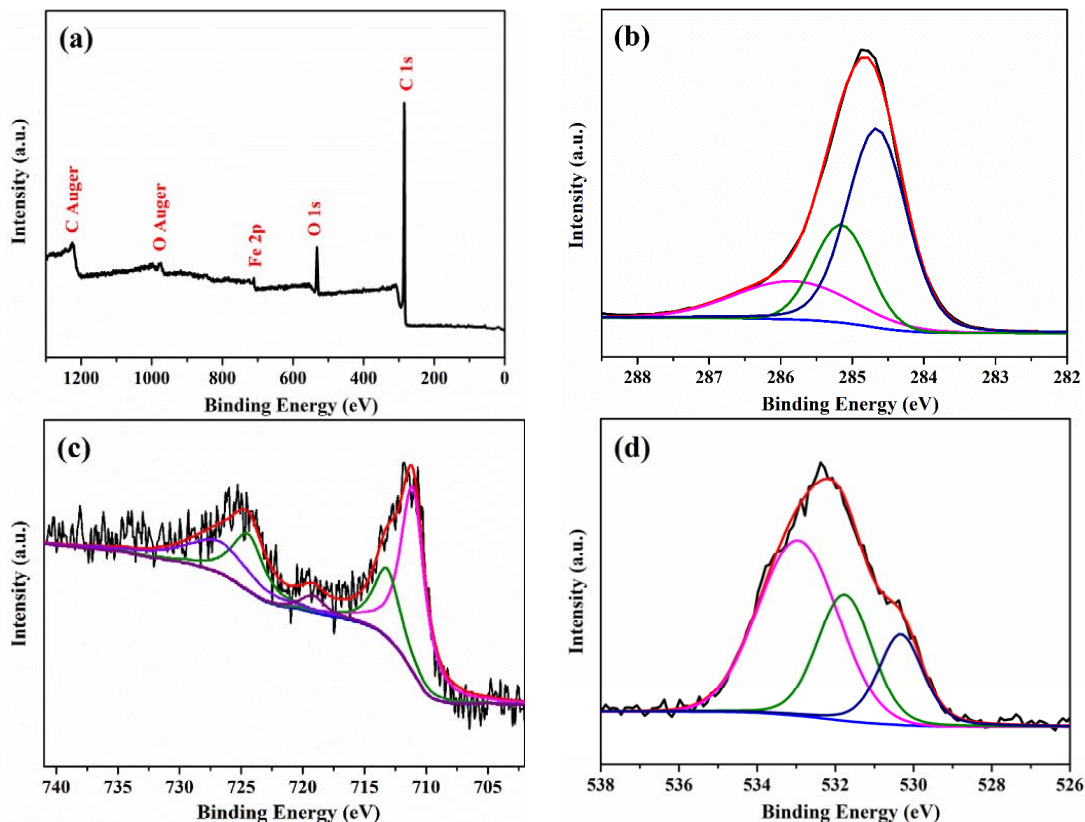


Figure 6. (a) XPS survey spectrum; high-resolution XPS spectra of (b) C 1s; (c) Fe 2p and (d) O 1s for CBC-Fe(II).

3.2. Batch Adsorption Studies

3.2.1. Effect of Adsorbent Dosage on Adsorption of RhB

To find the optimal adsorbent dosage, the effect of adsorbent dosage on removal efficiency of RhB by CBC-Fe(II) was investigated using 100, 200 and 600 mg/L as the initial dye concentrations. From the results presented in Figure 7, it can be seen that for various initial dye concentrations, the removal efficiency increased rapidly with increasing amounts of CBC-Fe(II) from 10 mg to 30 mg. It was because more accessible reactive sites are available to facilitate the dye adsorption process. However, when further increasing the amount of adsorbent from 30 mg to 50 mg, the required adsorption sites were getting closer to saturation, thus the removal efficiency only increased slightly. Thus, considering both the efficient removal of dye molecules and economic benefits, the optimal amount of the CBC-Fe(II) dosage was 30 mg.

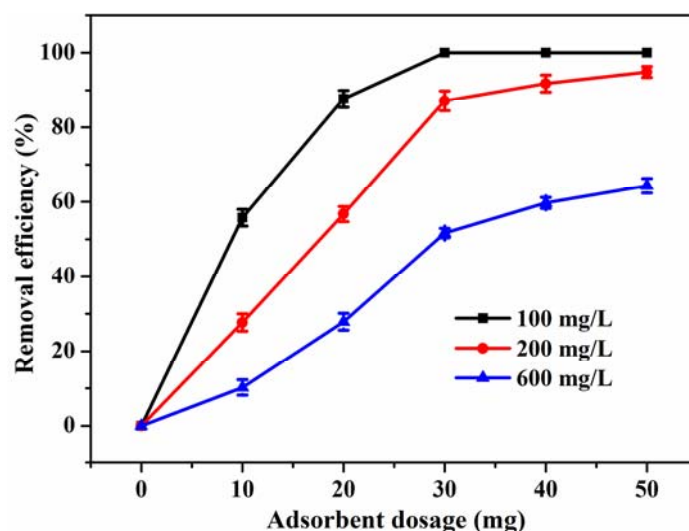


Figure 7. The influence of adsorbent dosage on removal efficiency of RhB by CBC-Fe(II).

3.2.2. Effect of Contact Time on Adsorption of RhB

Figure 8 shows the influence of reaction time on the removal efficiency of RhB by CBC, CBC-Fe(III) and CBC-Fe(II) under the same reaction temperature. The results obtained revealed that the removal efficiency of CBC-Fe(II) to RhB was much higher than that of CBC and CBC-Fe(III), demonstrating that CBC-Fe(II) possessed a relatively strong driving force on RhB. It was evidently observed that the removal efficiency of the three samples to RhB increased quickly during the initial stage, which was attributed to the free adsorption sites available for a large number of dye molecules. However, with the increase in contact time, the number of adsorption positions gradually decreased, leading to a slower adsorption rate. Finally, the adsorption equilibrium was achieved after 120 min, when the removal efficiency became almost constant.

3.2.3. Effect of Temperature on Adsorption of RhB

Figure 9 exhibited the effect of temperature on removal efficiency of RhB using CBC-Fe(II). It could be facily observed that the removal efficiency of CBC-Fe(II) towards RhB remained the same at different temperatures (15 °C, 25 °C and 35 °C). Therefore, for the sake of saving energy and costs, 25 °C was chosen as the adsorption temperature throughout the whole experiment.

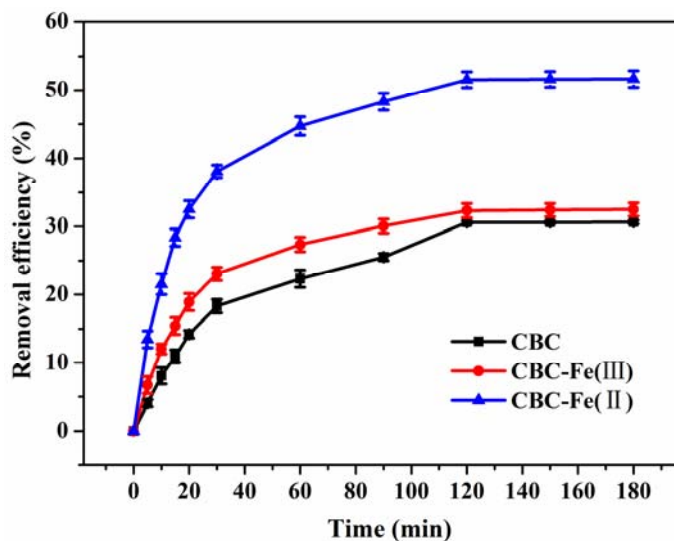


Figure 8. The influence of contact time on removal efficiency of RhB by CBC, CBC-Fe(III) and CBC-Fe(II) (adsorbent dosage: 30 mg; initial dye concentration: 600 mg/L).

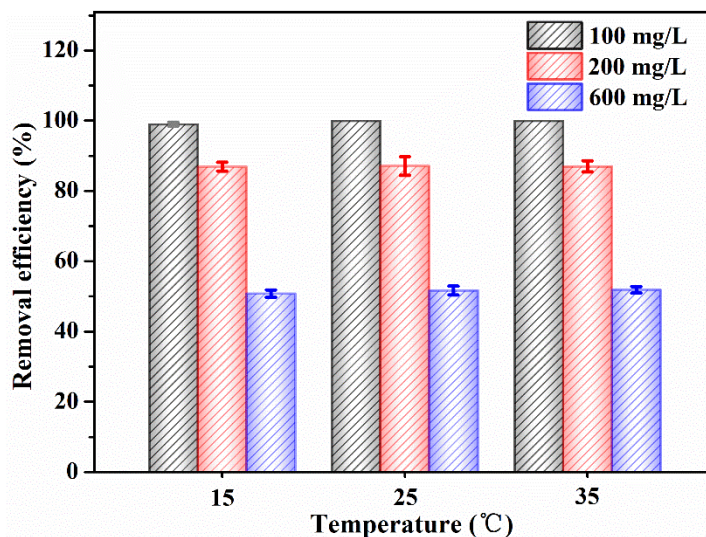


Figure 9. The influence of temperature on removal efficiency of RhB by CBC-Fe(II) (adsorbent dosage: 30 mg).

3.3. Kinetic and Isotherm Adsorption

3.3.1. Adsorption Kinetic Models

The adsorption kinetics of RhB onto CBC, CBC-Fe(III) and CBC-Fe(II) were investigated using pseudo-first-order and pseudo-second-order kinetic models, and the results are shown in Figure 10a. The adsorption kinetic models can be expressed as Equations (4) and (5), respectively:

$$Q_t = Q_e(1 - \exp(-K_1t)) \tag{4}$$

$$Q_t = \frac{K_2Q_e^2t}{1 + K_2Q_e t} \tag{5}$$

where Q_e (mg/g) and Q_t (mg/g) represent the quantity of RhB adsorbed on the adsorbent at the equilibrium and arbitrarily given time t (min), respectively. K_1 (1/min) and K_2 (g/(mg·min)) are adsorption rate constants of the pseudo-first-order and pseudo-second-order, respectively.

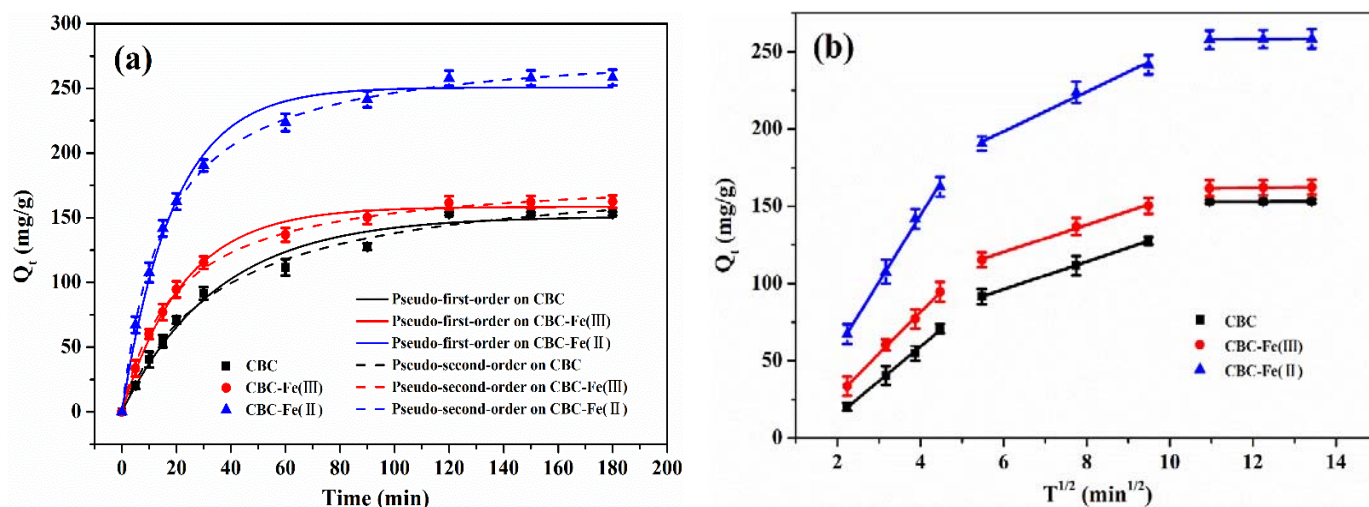


Figure 10. (a) Pseudo-first-order and pseudo-second-order and (b) intra-particle diffusion models of RhB adsorption by CBC, CBC-Fe(III) and CBC-Fe(II).

The related kinetic parameters of the above two models were obtained and are listed in Table 2. It was observed that for the three samples, the coefficients of correlation (R^2) were higher for the pseudo-second-order than that of the pseudo-first-order kinetic model, indicating that the pseudo-second-order kinetic model was more appropriate to describe the adsorption behavior towards RhB. The result implied that the dye adsorption process by the biochars was mainly dominated by chemical adsorption. Moreover, the theoretical adsorption capacity of CBC-Fe(II) was 284.9 mg/g, which was much higher than that of CBC (186.3 mg/g) and CBC-Fe(III) (184.1 mg/g), showing the best adsorption performance of CBC-Fe(II).

Table 2. Kinetic models parameters for RhB adsorption by CBC, CBC-Fe(III) and CBC-Fe(II).

Sample	Q_e , Experimental (mg/g)	Pseudo-First-Order			Pseudo-Second-Order		
		K_1 (1/min)	Q_e , Model (mg/g)	R^2	K_2 (g/(mg·min))	Q_e , Model (mg/g)	R^2
CBC	153.2	0.028	151.1	0.985	0.000154	186.3	0.992
CBC-Fe(III)	162.4	0.044	158.5	0.993	0.000273	184.1	0.998
CBC-Fe(II)	258.3	0.053	250.7	0.990	0.000226	284.9	0.999

Additionally, the intra-particle diffusion model (Figure 10b) was used to further evaluate the different stages of adsorption rate, which can be expressed as Equation (6).

$$Q_t = K_{id}t^{1/2} + c \tag{6}$$

where Q_t (mg/g) represents the quantity of RhB adsorbed on the adsorbent at arbitrarily given time t (min). K_{id} (mg/(g·min^{1/2})) is the diffusion rate constant. Constant c is the thickness of boundary layer.

From Figure 10b and Table 3, it is shown that for the three samples, all the lines did not pass through the origin, indicating that the intra-particle diffusion process was not the only rate-controlling mechanism for the adsorption system. The RhB adsorption process was comprised by three stages. In the first stage, the sharp rise was due to the liquid film diffusion process, while the second stage ascended more slowly, which represented the intra-particle diffusion process. The last equilibrium stage was attributed to the adsorption of dye molecules on the interior surface of adsorbents.

Table 3. Intra-particle diffusion model parameters for RhB adsorption by CBC, CBC-Fe(III) and CBC-Fe(II).

Sample	First Linear Segment		Second Linear Segment		Third Linear Segment	
	K_{id} ($mg/(g \cdot min^{1/2})$)	R^2	K_{id} ($mg/(g \cdot min^{1/2})$)	R^2	K_{id} ($mg/(g \cdot min^{1/2})$)	R^2
CBC	22.339	0.995	8.965	0.999	0.074	0.905
CBC-Fe(III)	26.962	0.998	8.783	0.994	0.348	0.994
CBC-Fe(II)	43.337	0.996	12.831	0.981	0.224	0.998

3.3.2. Adsorption Isotherm Models

In order to study the interactive behavior between adsorbates and adsorbents, the equilibrium adsorption isotherms of RhB adsorption by CBC, CBC-Fe(III) and CBC-Fe(II) were described by the Langmuir and Freundlich isotherm models, and the results are presented in Figure 11. The two isotherm models can be expressed as Equations (7) and (8).

$$Q_e = \frac{Q_m K_L C_e}{1 + K_L C_e} \tag{7}$$

$$Q_e = K_F C_e^{1/n} \tag{8}$$

where C_e (mg/L) is the equilibrium concentration of dye solution, Q_e (mg/g) and Q_m (mg/g) represent equilibrium adsorption capacity and maximum adsorption capacity of CBC-Fe(II), respectively. K_L (L/mg) and K_F [(mg/g)(mg/L)^{1/n}] represent the constants of the Langmuir and Freundlich isotherms and n is the linearity index of adsorption intensity.

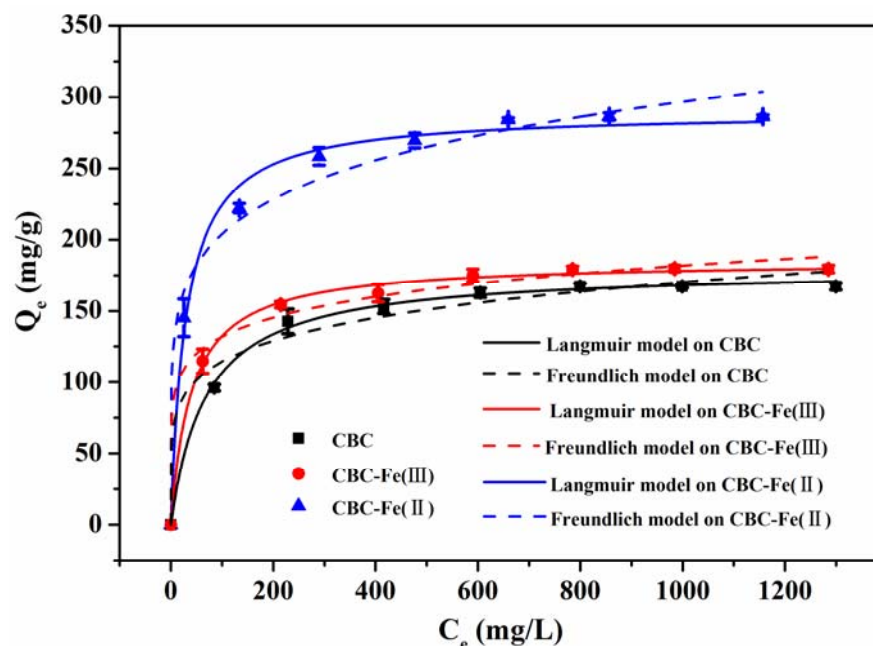


Figure 11. Langmuir and Freundlich isotherms of RhB adsorption by CBC, CBC-Fe(III) and CBC-Fe(II).

It was observed from Figure 11 that the quantity of RhB adsorbed by CBC, CBC-Fe(III) and CBC-Fe(II) increased rapidly at low concentrations, then gradually approached the saturated adsorption capacity. The experimental data were fitted by the Langmuir and the Freundlich models, and the calculated parameters are described in Table 4. Apparently, for the three samples, the significant correlation coefficient value of Langmuir isotherm model was higher than that of the Freundlich isotherm model. The result indicated that the Langmuir isotherm model was superior for revealing the adsorption process, suggesting the equilibrium adsorption mechanism of RhB by CBC, CBC-Fe(III) and CBC-Fe(II) was more

inclined to monolayer adsorption. Furthermore, the maximum adsorption capacity (Q_m) for CBC, CBC-Fe(III) and CBC-Fe(II) obtained by the Langmuir model was 179.7 mg/g, 185.1 mg/g and 289.6 mg/g, respectively, which were close to the experimental values of 167.4 mg/g, 179.7 mg/g and 286.4 mg/g, respectively. It is worth noting that the CBC-Fe(II) adsorbent prepared in this study was found to show obvious advantages compared with biochars for RhB removal synthesized in other studies (Table 5).

Table 4. Parameters derived from isotherms of RhB adsorption by CBC, CBC-Fe(III) and CBC-Fe(II).

Sample	Langmuir			Freundlich		
	Q_m (mg/g)	K_L (L/mg)	R^2	K_F [(mg/g)(mg/L) ^{1/n}]	n	R^2
CBC	179.7	0.0145	0.998	51.785	5.808	0.972
CBC-Fe(III)	185.1	0.0250	0.998	69.732	7.212	0.988
CBC-Fe(II)	289.6	0.0343	0.992	96.384	6.144	0.982

Table 5. Comparison of the adsorption capacity of RhB with other biochar adsorbents reported in the literature.

Biochar	Biomass	Q_m (mg/g)	References
biochar	cassava slag	105.3	[25]
BHC-800	bamboo shoot shell	85.8	[26]
sulfur-doped biochar	tapioca peel waste	33.1	[27]
earthworm manure derived biochar	earthworm manure	21.6	[49]
plantain peel activated biochar	plantain peel	84.4	[50]
magnetic chicken bone-based biochar	chicken bone	96.5	[51]
Fe–N co-modified biochar	coconut shell	12.4	[52]
magnetic biochar (AMBC)	Rice straw	53.7	[53]
CBC-Fe(II)	<i>Chlorella vulgaris</i>	286.4	This study

3.4. Regeneration and Reusability of CBC-Fe(II)

To investigate the regeneration and reusability of CBC-Fe(II), the adsorption experiment was conducted in five consecutive cycles. After each adsorption experiment, the adsorbent was recollected by a magnet and washed with absolute ethyl alcohol and ultra-pure water, respectively. For the next adsorption cycle, 25 mL of RhB solution was added to CBC-Fe(II). The results of repetitive use of the adsorbent for RhB removal are shown in Figure 12. It can be seen that the regeneration efficiency of the CBC-Fe(II) decreased with each recycling process, which might be due to the increased RhB residual on the adsorbent surface. However, CBC-Fe(II) still possessed a certain adsorption capacity towards RhB after five adsorption cycles.

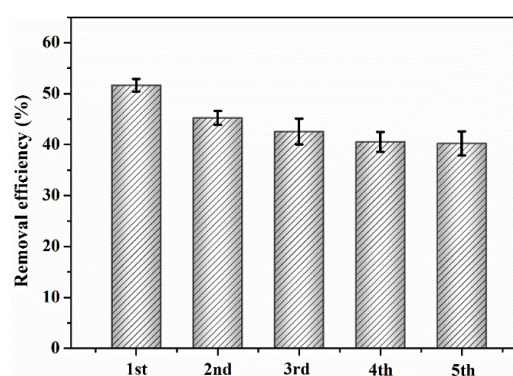


Figure 12. Recycling test of RhB adsorption by CBC-Fe(II) (adsorbent dosage: 30 mg, initial dye concentration: 600 mg/L).

4. Conclusions

In summary, a magnetically separable nano iron oxide–modified biochar (CBC-Fe(II)) was fabricated via a facile hydrothermal-pyrolyzing method. The synthesized CBC-Fe(II) adsorbent with a high surface area exhibited excellent magnetic properties and could be simply collected by a magnet. Compared with CBC and CBC-Fe(III), CBC-Fe(II) showed powerful adsorption performance for removing RhB from water. The RhB was optimally adsorbed at a CBC-Fe(II) dosage of 30 mg, with a contact time of 120 min and temperature of 25 °C. The adsorption process of RhB onto CBC-Fe(II) was found to obey the pseudo-second-order model and the Langmuir isotherm model well. Furthermore, the fitting results of the intra-particle diffusion model indicated that intraparticle diffusion was not the sole rate-controlling step as liquid film diffusion and interior surface adsorption also regulated the adsorption rate. All the results revealed that the prepared CBC-Fe(II) adsorbent possessed high potential in environmental remediation for dye removal.

Author Contributions: Conceptualization, X.Z.; validation, X.C.; formal analysis, Z.F.G.; investigation, S.W. and S.D.; data curation, Z.F. and X.L.; writing—original draft preparation, Z.P.; writing—review and editing, Z.P., Z.F. and X.C.; supervision, W.H.; project administration, Y.S.; funding acquisition, X.C., X.Z., Z.F.G. and Y.S. All authors have read and agreed to the published version of the manuscript.

Funding: This research was funded by the National Natural Science Foundation of China, grant numbers 51979011 and 52179122; the Central Non-Profit Scientific Research Fund for Institutes, grant numbers CKSF2021483/CL, CKSF2021437/CL and CKSF2021430/CL; the Knowledge Innovation Program of Wuhan-Basic Research, grant number CKSD2022360/CL; and the Jiangxi Academy of Qater Science and Engineering Open Project Fund, grant number 2021SKSG04.

Institutional Review Board Statement: Not applicable.

Informed Consent Statement: Not applicable.

Data Availability Statement: The data presented in this study are available on request from the corresponding authors.

Acknowledgments: The authors gratefully acknowledge the support from the National Natural Science Foundation of China (No. 51979011 and 52179122), the Central Non-Profit Scientific Research Fund for Institutes (No. CKSF2021483/CL, CKSF2021437/CL and CKSF2021430/CL), the Knowledge Innovation Program of Wuhan-Basic Research (No. CKSD2022360/CL) and the Jiangxi Academy of Qater Science and Engineering Open Project Fund (No. 2021SKSG04).

Conflicts of Interest: The authors declare no conflict of interest.

References

1. Zhang, J.; Liu, H.; Gao, W.; Cheng, D.; Tan, F.; Wang, W.; Wang, X.; Qiao, X.; Wong, P.K.; Yao, Y. In situ zinc cyanamide coordination induced highly N-rich graphene for efficient peroxymonosulfate activation. *J. Mater. Chem. A* **2022**, *10*, 12016–12025. [[CrossRef](#)]
2. Chen, P.; Dong, N.; Zhang, J.; Wang, W.; Tan, F.; Wang, X.; Qiao, X.; Wong, P.K. Investigation on visible-light photocatalytic performance and mechanism of zinc peroxide for tetracycline degradation and *Escherichia coli* inactivation. *J. Colloid Interface Sci.* **2022**, *624*, 137–149. [[CrossRef](#)] [[PubMed](#)]
3. Dong, N.; Ge, L.; Chen, P.; Wang, W.; Tan, F.; Wang, X.; Qiao, X.; Wong, P.K. Non-radical activation of CaO₂ nanoparticles by MgNCN/MgO composites for efficient remediation of organic and heavy metal-contaminated wastewater. *Sep. Purif. Technol.* **2022**, *285*, 120334. [[CrossRef](#)]
4. Dong, N.; Wu, D.; Ge, L.; Wang, W.; Tan, F.; Wang, X.; Qiao, X.; Wong, P.K. Constructing a brand-new advanced oxidation process system composed of MgO₂ nanoparticles and MgNCN/MgO nanocomposites for organic pollutant degradation. *Environ. Sci. Nano* **2022**, *9*, 335–348. [[CrossRef](#)]
5. Ouachtak, H.; El Haouti, R.; El Guerdaoui, A.; Haounati, R.; Amaterz, E.; Addi, A.A.; Akbal, F.; Taha, M.L. Experimental and molecular dynamics simulation study on the adsorption of Rhodamine B dye on magnetic montmorillonite composite γ -Fe₂O₃@Mt. *J. Mol. Liq.* **2020**, *309*, 113142. [[CrossRef](#)]
6. Li, Y.; Du, Q.; Liu, T.; Sun, J.; Wang, Y.; Wu, S.; Wang, Z.; Xia, Y.; Xia, L. Methylene blue adsorption on graphene oxide/calcium alginate composites. *Carbohydr. Polym.* **2013**, *95*, 501–507. [[CrossRef](#)]
7. Hussein, T.K.; Jasim, N.A. A comparison study between chemical coagulation and electro-coagulation processes for the treatment of wastewater containing reactive blue dye. *Mater. Today* **2021**, *42*, 1946–1950. [[CrossRef](#)]

8. Li, S.; Kang, Y. Effect of PO_4^{3-} on the polymerization of polyferric phosphatic sulfate and its flocculation characteristics for different simulated dye wastewater. *Sep. Purif. Technol.* **2021**, *276*, 119373. [[CrossRef](#)]
9. Paździor, K.; Bilińska, L.; Ledakowicz, S. A review of the existing and emerging technologies in the combination of AOPs and biological processes in industrial textile wastewater treatment. *Chem. Eng. J.* **2019**, *376*, 120597. [[CrossRef](#)]
10. Shrestha, D. Efficiency of wood-dust of dalbergia sisoo as low-cost adsorbent for Rhodamine-B dye removal. *Nanomaterials* **2021**, *11*, 2217. [[CrossRef](#)]
11. Sun, L.; Mo, Y.; Zhang, L. A mini review on bio-electrochemical systems for the treatment of azo dye wastewater: State-of-the-art and future prospects. *Chemosphere* **2022**, *294*, 133801. [[CrossRef](#)] [[PubMed](#)]
12. de Almeida, E.J.R.; Mazzeo, D.E.C.; Sommaggio, L.R.D.; Marin-Morales, M.A.; de Andrade, A.R.; Corso, C.R. Azo dyes degradation and mutagenicity evaluation with a combination of microbiological and oxidative discoloration treatments. *Ecotox. Environ. Saf.* **2019**, *183*, 109484. [[CrossRef](#)]
13. Nozad, E.; Poursattar Marjani, A.; Mahmoudian, M. A novel and facile semi-IPN system in fabrication of solvent resistant nano-filtration membranes for effective separation of dye contamination in water and organic solvents. *Sep. Purif. Technol.* **2022**, *282*, 120121. [[CrossRef](#)]
14. Zhang, J.; Hu, X.; Yan, X.; Feng, R.; Zhou, M.; Xue, J. Enhanced adsorption of Rhodamine B by magnetic nitrogen-doped porous carbon prepared from bimetallic ZIFs. *Colloid. Surf. A* **2019**, *575*, 10–17. [[CrossRef](#)]
15. Zhang, H.; Shi, X.; Li, J.; Kumar, P.; Liu, B. Selective dye adsorption by zeolitic imidazolate framework-8 loaded UiO-66-NH_2 . *Nanomaterials* **2019**, *9*, 1283. [[CrossRef](#)] [[PubMed](#)]
16. Elkartehi, M.E.; Mahmoud, R.; Shehata, N.; Farghali, A.; Gamil, S.; Zaher, A. LDH nanocubes synthesized with zeolite templates and their high performance as adsorbents. *Nanomaterials* **2021**, *11*, 3315. [[CrossRef](#)]
17. Ain, Q.U.; Rasheed, U.; Yaseen, M.; Zhang, H.; He, R.; Tong, Z. Fabrication of magnetically separable 3-acrylamidopropyltrimethylammonium chloride intercalated bentonite composite for the efficient adsorption of cationic and anionic dyes. *Appl. Surf. Sci.* **2020**, *514*, 145929. [[CrossRef](#)]
18. Paton-Carrero, A.; Sanchez, P.; Sánchez-Silva, L.; Romero, A. Graphene-based materials behaviour for dyes adsorption. *Mater. Today Commun.* **2022**, *30*, 103033. [[CrossRef](#)]
19. Wang, H.; Li, Z.; Yahyaoui, S.; Hanafy, H.; Seliem, M.K.; Bonilla-Petriciolet, A.; Luiz Dotto, G.; Sellaoui, L.; Li, Q. Effective adsorption of dyes on an activated carbon prepared from carboxymethyl cellulose: Experiments, characterization and advanced modelling. *Chem. Eng. J.* **2021**, *417*, 128116. [[CrossRef](#)]
20. Chabi, N.; Baghdadi, M.; Sani, A.H.; Golzary, A.; Hosseinzadeh, M. Removal of tetracycline with aluminum boride carbide and boehmite particles decorated biochar derived from algae. *Bioresour. Technol.* **2020**, *316*, 123950. [[CrossRef](#)]
21. Binda, G.; Spanu, D.; Bettinetti, R.; Magagnin, L.; Pozzi, A.; Dossi, C. Comprehensive comparison of microalgae-derived biochar from different feedstocks: A prospective study for future environmental applications. *Algal Res.* **2020**, *52*, 102103. [[CrossRef](#)]
22. Yu, K.L.; Lee, X.J.; Ong, H.C.; Chen, W.-H.; Chang, J.-S.; Lin, C.-S.; Show, P.L.; Ling, T.C. Adsorptive removal of cationic methylene blue and anionic Congo red dyes using wet-torrefied microalgal biochar: Equilibrium, kinetic and mechanism modeling. *Environ. Pollut.* **2021**, *272*, 115986. [[CrossRef](#)] [[PubMed](#)]
23. Fan, Z.; Li, J.; Zhou, Y.; Fu, Q.; Yang, W.; Zhu, X.; Liao, Q. A green, cheap, high-performance carbonaceous catalyst derived from *Chlorella pyrenoidosa* for oxygen reduction reaction in microbial fuel cells. *Int. J. Hydrogen Energ.* **2017**, *42*, 27657–27665. [[CrossRef](#)]
24. Fan, Z.; Li, J.; Yang, W.; Fu, Q.; Sun, K.; Song, Y.-C.; Wei, Z.; Liao, Q.; Zhu, X. Green and facile synthesis of iron oxide nanoparticle-embedded N-doped biocarbon as an efficient oxygen reduction electrocatalyst for microbial fuel cells. *Chem. Eng. J.* **2020**, *385*, 123393. [[CrossRef](#)]
25. Wu, J.; Yang, J.; Huang, G.; Xu, C.; Lin, B. Hydrothermal carbonization synthesis of cassava slag biochar with excellent adsorption performance for Rhodamine B. *J. Clean. Prod.* **2020**, *251*, 119717. [[CrossRef](#)]
26. Hou, Y.; Huang, G.; Li, J.; Yang, Q.; Huang, S.; Cai, J. Hydrothermal conversion of bamboo shoot shell to biochar: Preliminary studies of adsorption equilibrium and kinetics for Rhodamine B removal. *J. Anal. Appl. Pyrol.* **2019**, *143*, 104694. [[CrossRef](#)]
27. Vigneshwaran, S.; Sirajudheen, P.; Karthikeyan, P.; Meenakshi, S. Fabrication of sulfur-doped biochar derived from tapioca peel waste with superior adsorption performance for the removal of Malachite green and Rhodamine B dyes. *Surf. Interfaces* **2021**, *23*, 100920. [[CrossRef](#)]
28. Qu, J.; Shi, J.; Wang, Y.; Tong, H.; Zhu, Y.; Xu, L.; Wang, Y.; Zhang, B.; Tao, Y.; Dai, X.; et al. Applications of functionalized magnetic biochar in environmental remediation: A review. *J. Hazard. Mater.* **2022**, *434*, 128841. [[CrossRef](#)]
29. Geng, J.; Gu, F.; Chang, J. Fabrication of magnetic lignosulfonate using ultrasonic-assisted in situ synthesis for efficient removal of Cr(VI) and Rhodamine B from wastewater. *J. Hazard. Mater.* **2019**, *375*, 174–181. [[CrossRef](#)]
30. Lin, C.-R.; Ivanova, O.S.; Edelman, I.S.; Knyazev, Y.V.; Zharkov, S.M.; Petrov, D.A.; Sokolov, A.E.; Svetlitsky, E.S.; Velikanov, D.A.; Solovyov, L.A.; et al. Carbon double coated Fe_3O_4 @C@C nanoparticles: Morphology features, magnetic properties, dye adsorption. *Nanomaterials* **2022**, *12*, 376. [[CrossRef](#)]
31. Trinh, B.-S.; Le, P.T.K.; Werner, D.; Phuong, N.H.; Luu, T.L. Rice husk biochars modified with magnetized iron oxides and nano zero valent iron for decolorization of dyeing wastewater. *Processes* **2019**, *7*, 660. [[CrossRef](#)]
32. Singh, A.; Sharma, R.; Pant, D.; Malaviya, P. Engineered algal biochar for contaminant remediation and electrochemical applications. *Sci. Total Environ.* **2021**, *774*, 145676. [[CrossRef](#)]

33. Lalmunsiam; Gupta, P.L.; Jung, H.; Tiwari, D.; Kong, S.-H.; Lee, S.-M. Insight into the mechanism of Cd(II) and Pb(II) removal by sustainable magnetic biosorbent precursor to *Chlorella vulgaris*. *J. Taiwan Inst. Chem. Eng.* **2017**, *71*, 206–213. [[CrossRef](#)]
34. Yoon, K.; Cho, D.-W.; Wang, H.; Song, H. Co-pyrolysis route of *Chlorella* sp. and bauxite tailings to fabricate metal-biochar as persulfate activator. *Chem. Eng. J.* **2022**, *428*, 132578. [[CrossRef](#)]
35. Amin, M.; Chetpattananondh, P.; Khan, M.N. Ultrasound assisted adsorption of reactive dye-145 by biochars from marine *Chlorella* sp. extracted solid waste pyrolyzed at various temperatures. *J. Environ. Chem. Eng.* **2020**, *8*, 104403. [[CrossRef](#)]
36. Amin, M.; Chetpattananondh, P. Biochar from extracted marine *Chlorella* sp. residue for high efficiency adsorption with ultrasonication to remove Cr(VI), Zn(II) and Ni(II). *Bioresour. Technol.* **2019**, *289*, 121578. [[CrossRef](#)]
37. Ajiboye, T.O.; Oyewo, O.A.; Onwudiwe, D.C. Adsorption and photocatalytic removal of Rhodamine B from wastewater using carbon-based materials. *FlatChem* **2021**, *29*, 100277. [[CrossRef](#)]
38. Xue, S.; Tu, B.; Li, Z.; Ma, X.; Xu, Y.; Li, M.; Fang, C.; Tao, H. Enhanced adsorption of Rhodamine B over *Zoysia sinica* Hance-based carbon activated by ammonium chloride and sodium hydroxide treatments. *Colloid. Surf. A* **2021**, *618*, 126489. [[CrossRef](#)]
39. Guimarães, T.; Luciano, V.A.; Silva, M.S.V.; de Carvalho Teixeira, A.P.; da Costa, M.M.; Lopes, R.P. Biochar-iron composites: An efficient material for dyes removal. *Environ. Nanotechnol. Monit. Manag.* **2022**, *17*, 100645. [[CrossRef](#)]
40. Lu, Y.; Chen, J.; Zhao, L.; Zhou, Z.; Qiu, C.; Li, Q. Adsorption of Rhodamine B from aqueous solution by goat manure biochar: Kinetics, isotherms, and thermodynamic studies. *Pol. J. Environ. Stud.* **2020**, *29*, 2721–2730. [[CrossRef](#)]
41. Ye, L.; Wang, R.; Ji, G.; Wu, H.; Qu, H.; Wang, L.; Liu, J. From green tide to biochar: Thermal decomposition kinetics and TG-FTIR study of microalgae from Chaohu Lake. *Int. J. Energy Res.* **2020**, *45*, 8083–8090. [[CrossRef](#)]
42. Xu, S.; Chen, J.; Peng, H.; Leng, S.; Li, H.; Qu, W.; Hu, Y.; Li, H.; Jiang, S.; Zhou, W.; et al. Effect of biomass type and pyrolysis temperature on nitrogen in biochar, and the comparison with hydrochar. *Fuel* **2021**, *291*, 120128. [[CrossRef](#)]
43. Fouad, D.E.; Zhang, C.; El-Didamony, H.; Yingnan, L.; Mekuria, T.D.; Shah, A.H. Improved size, morphology and crystallinity of hematite (α -Fe₂O₃) nanoparticles synthesized via the precipitation route using ferric sulfate precursor. *Results Phys.* **2019**, *12*, 1253–1261. [[CrossRef](#)]
44. Zhu, Z.; Huang, C.P.; Zhu, Y.; Wei, W.; Qin, H. A hierarchical porous adsorbent of nano- α -Fe₂O₃/Fe₃O₄ on bamboo biochar (HPA-Fe/C-B) for the removal of phosphate from water. *J. Water Process Eng.* **2018**, *25*, 96–104. [[CrossRef](#)]
45. Bogireddy, N.K.R.; Cruz Silva, R.; Valenzuela, M.A.; Agarwal, V. 4-nitrophenol optical sensing with N doped oxidized carbon dots. *J. Hazard. Mater.* **2020**, *386*, 121643. [[CrossRef](#)]
46. Chenakin, S.; Kruse, N. XPS characterization of transition metal oxalates. *Appl. Surf. Sci.* **2020**, *515*, 146041. [[CrossRef](#)]
47. Peng, Z.; Wu, D.; Wang, W.; Tan, F.; Ng, T.W.; Chen, J.; Qiao, X.; Wong, P.K. Fabrication of magnetic Fe@ZnO_{0.6}S_{0.4} nanocomposite for visible-light-driven photocatalytic inactivation of *Escherichia coli*. *Appl. Surf. Sci.* **2017**, *396*, 19–25. [[CrossRef](#)]
48. Chen, D.; He, D.; Lu, J.; Zhong, L.; Liu, F.; Liu, J.; Yu, J.; Wan, G.; He, S.; Luo, Y. Investigation of the role of surface lattice oxygen and bulk lattice oxygen migration of cerium-based oxygen carriers: XPS and designed H₂-TPR characterization. *Appl. Catal. B Environ.* **2017**, *218*, 249–259. [[CrossRef](#)]
49. Wang, Z.; Shen, D.; Shen, F.; Wu, C.; Gu, S. Kinetics, equilibrium and thermodynamics studies on biosorption of Rhodamine B from aqueous solution by earthworm manure derived biochar. *Int. Biodeter. Biodegr.* **2017**, *120*, 104–114. [[CrossRef](#)]
50. Adekola, F.A.; Ayodele, S.B.; Inyinbor, A.A. Activated biochar prepared from plaintain peels: Characterization and Rhodamine B adsorption data set. *Chem. Data Collect.* **2019**, *19*, 100170. [[CrossRef](#)]
51. Ajayi, O.A.; Nisar, N.; Ifebajo, A.O.; Oladipo, A.A. High-performance magnetic chicken bone-based biochar for efficient removal of rhodamine-B dye and tetracycline: Competitive sorption analysis. *Water Sci. Technol.* **2017**, *76*, 373–385.
52. Li, X.; Shi, J.; Luo, X. Enhanced adsorption of Rhodamine B from water by Fe-N co-modified biochar: Preparation, performance, mechanism and reusability. *Bioresour. Technol.* **2022**, *343*, 126103. [[PubMed](#)]
53. Ren, Z.; Chen, F.; Wang, B.; Song, Z.; Zhou, Z.; Ren, D. Magnetic biochar from alkali-activated rice straw for removal of Rhodamine B from aqueous solution. *Environ. Eng. Res.* **2019**, *25*, 536–544.